Semiconductor-Metal Nano-Floret Hybrid Structures by Self-Processing Synthesis

Ori Hazut[1‡], Sharon Waichman[1‡], Thangavel Subramani[1†], Debabrata Sarkar[1], Sthitaprajna Dash[1], Teresa Roncal-Herrero[2], Roland Kröger[2], and Roie Yerushalmi[1]*

[1] Institute of Chemistry and the Center for Nanoscience and Nanotechnology, The Hebrew University of Jerusalem, Edmond J. Safra Campus, Givat Ram, Jerusalem, 91904, Israel.

[2] Department of Physics, University of York, Heslington, York YO10 5DD, United Kingdom.

ABSTRACT: We present a synthetic strategy that takes advantage of the inherent asymmetry exhibited by semiconductor nanowires prepared by Au-catalyzed chemical vapor deposition (CVD). The metal-semiconductor junction is used for activating etch, deposition, and modification steps localized to the tip area using a wet-chemistry approach. The hybrid nanostructures obtained for the coinage metals Cu, Ag, and Au resemble the morphology of grass flowers, termed here Nano-floret hybrid nanostructures consisting of a high aspect ratio SiGe nanowire (NW) with a metallic nanoshell cap. The synthetic method is used to prepare hybrid nanostructures in one step by triggering a programmable cascade of events that is autonomously executed, termed self-processing synthesis. The synthesis progression was monitored by *ex situ* transmission electron microscopy (TEM), *in situ* scanning transmission electron microscopy (STEM) and inductively coupled plasma mass spectrometry (ICP-MS) analyses to study the mechanistic reaction details of the various processes taking place during the synthesis. Our results indicate that the synthesis involve distinct processing steps including localized oxide etch, metal deposition, and process termination. Control over the deposition and etching processes is demonstrated by several parameters: (i) etchant concentration (water), (ii) SiGe alloy composition, (iii) reducing agent, (iv) metal redox potential, and (v) addition of surfactants for controlling the deposited metal grain size. The NF structures exhibit broad plasmonic absorption that is utilized for demonstrating surface-enhanced raman scattering (SERS) of thiophenol monolayer. The new type of nanostructures feature a metallic nanoshell directly coupled to the crystalline semiconductor NW showing broad plasmonic absorption.

Bottom-up and top-down approaches are often used to construct nanosystems that are comprised of two or more components with distinct chemical compositions, structural domains and physical properties, which are commonly referred to as hybrid nanostructures (HNS).[1–7] Overall, HNS are central for designing novel materials with desired optical, mechanical, and electronic properties at the nanometer scale by introducing architectures with programmed compositions and heterogeneous shapes. It is important to combine several materials and morphologies within the same nanostructure to attain new and synergistic functionalities because properties at the nanoscale depend on the composition, size, and dimensionality of the nanostructures.[4] For example, the combination of semiconducting (SC) nanorods with metallic nanoparticles (NPs) improved light harvesting because of the enhanced absorbance and charge separation properties of the combined nanosystem relative to the individual components.[4] Such structures can be prepared using a large spectrum of approaches, including template-assisted synthesis, colloid surface chemistry, and protein assembly.[8–12] However, these approaches often suffer from limited and generally complex control over the synthesis parameters of the various system materials; thus, their synthesis development is typically time and cost intensive. Here, we demonstrate a novel bottom-up synthetic approach for preparing semiconductor-metal HNSs that consist of a high aspect ratio SiGe nanowire (NW) with a metallic cap (Cu, Ag, and Au) deposited at the NW tip, where the Au catalyst used for chemical vapor deposition (CVD) synthesis of the NW is utilized for triggering the synthesis which is confined to the NW tip. Such hybrid nanostructures featuring SC-metal components where the SC is a SiGe alloy with adjustable composition and electronic properties and the metallic component is selected from the coinage metals (row 11 of the periodic table) are highly valuable for an array of applications including sensing, photocatalysis, and optics due to the unique properties exhibited by these systems. For example, DNA sensing was demonstrated using Ag-SiC system by spec-

troscopic modulation method,[13] hydrogen peroxide sensing was demonstrated using Ag-nanostrucutred Si wafers by electrochemical and surface-enhanced Raman scattering (SERS) methods[14] and Au-coated Si NWs were demonstrated as sensitive FET devices for the detection of sodium ions.[15] Furthermore, such structures are highly efficient as SERS substrates[14,16,17] for detection of a large range of organic molecules. Au-Si hybrid nanostructures were demonstrated as powerful platforms for gas sensing applications by utilizing the sharp nano-scale morphologies that result in the local electric fields enhancement.[18] The unique electronic structure which is formed at the metal-semiconductor interface for such systems was demonstrated for improving the photocatalytic performance, for example, for the degradation of various dyes[19,20] and for the photoconversion of formic acid into hydrogen and carbon dioxide.[19] In the optics field such structures were applied for realizing high quality factor waveguides,[21] negative index materials,[22] IR modulator,[23] photo-acoustic,[24] and plasmonics[25] based devices. The HNS prepared here exhibit desirable combination of aspect ratios and dimensions with the metallic tip dimensions in the range of tens to hundreds nanometers and the SC component with typically several tens of nanometer in diameter and up to tens of microns in length.

RESULTS AND DISCUSSION

The metal-SC hybrid morphologies obtained resemble grass flowers or 'florets' as presented in Figure 1 (inspired by the use of water for initiating the synthesis). Therefore, these structures were termed nano-floret (NF)-like structures. The process was studied using various water concentrations, different metals (Cu, Ag and Au), and different SiGe alloy compositions to deduce the roles of each factor and the respective mechanisms involved. Overall, *ex situ* transmission electron microscopy (TEM), *in situ* scanning transmission electron microscopy (STEM) using a novel fluid cell TEM holder and inductively coupled plasma mass spectrometry (ICP-MS) techniques were used to study the mechanistic reaction details and progression of the various processes. Our analyses provided structural and chemical information regarding the processes that occurred and explained the underlying mechanisms. The structural evolution with respect to the process parameters, such as water concentrations in the deposition solutions and the SiGe alloy composition, were studied using energy dispersive X-ray spectroscopy (EDS). In addition, ICP-MS analyses were performed on the process solutions to quantify the dissolved Ge levels as a function of the process parameters. The SC-Au nanoparticle (NP) junction present at the SiGe NW tip and originating from the CVD synthesis step set an inherent asymmetry in the NW electronic structure (see Figure S1 in the Supporting information, for calculated Au-SiGe junction band diagram). The Au-SC junction at the nanowire tip was further exploited for catalyzing both the SiGe oxide layer etching and for promoting metal deposition processes triggered by water as a mild etchant towards the native oxide of the SiGe alloy.
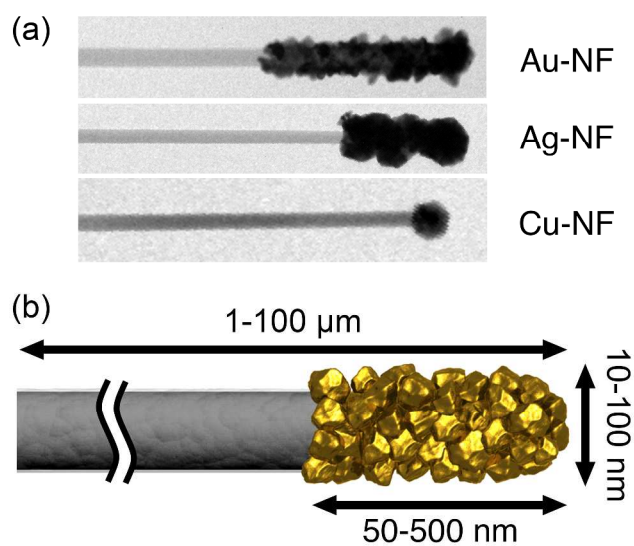

Figure 1. Transmission electron microscopy (TEM) of Nanofloret (NF) structures (a) obtained for SiGe NWs reacted with Cu, Ag, and Au featuring a stem (SiGe NW) and corona (deposited metal) at the tip region. (b) Typical dimensions for the NF structure, overall length of 1-100 microns resulting from the SiGe NWs used, deposited metal region is typically 10-100 nm in diameter and 50-500 nm long.

The structural evolution was quantified by measuring the head diameter (d_H, Figure 2b) and the metal deposition length at the tip area (L, Figure 2c).

Overall, d_H remained constant and was independent of the water concentration (d_H ~65 nm for the SiGe NWs diameter used). In contrast, the metal deposition length L at the SiGe NW surface abruptly increased to ~360 nm in water in EtOH concentrations greater than ~1.0 M (Figure 2c). A further increase of the water concentration did not result in further growth beyond 360 nm neck length, indicating a self-limiting process (Figure 2c). Additional representative TEM images and histograms showing the typical size distribution of cap diameter and length obtained for each water concentration are presented in detail in Figures S2-S7 in the Supporting information section. Representative low magnification, large scan area TEM images of the NF structures are presented in Figure S8.
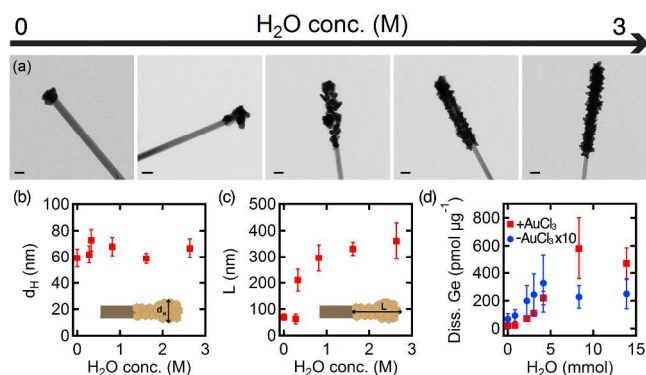
Figure 2. Water assisted growth of Au-NF. (a) Left to right: TEM images obtained for Au-NF prepared with specified water concentrations of 0, 0.28, 0.82, 1.62, and 2.64 M (scale bar is 50 nm). Quantification of Au cap deposition, (b) Au cap diameter (dH) and (c) Au cap length (L) as a function of water concentration. (d) Mass spectrometry (MS) analysis of the dissolved Ge obtained in the deposition solution containing the specified water concentration with 1 mM AuCl$_3$ (■) and without AuCl$_3$ (●, X10). Additional representative TEM images and histograms showing low magnification images, the typical size distribution of cap diameter and length obtained for each water concentration are presented in detail in Figures S2-S8 in the Supporting information section.

The structures of the fully evolved Au-NFs were further characterized by preparing cross-sectional focused ion beam (FIB) lamellae, which were subsequently analyzed using TEM, EDS, and scanning electron microscopy (SEM) at different regions of the structure (Figure S9 in the Supporting information). To quantify the dissolved Ge concentration as it evolves during the deposition process, ICP-MS was used for a range of water concentrations (Figure 2d). The dissolved Ge experiments were performed by immersing the SiGe NWs in EtOH with 1 mM AuCl$_3$ and using water concentrations in the range of 0.0 (anhydrous) to approx. 3.0 M. This process was termed a "deposition solution" process, whereas the repetition of the procedure with identical conditions and without the metal salt was called the "blank solution" process. The ICP-MS results indicate an increase in dissolved Ge concentrations with increased water addition (with saturation at approximately 8 mmol H$_2$O for both the blank and deposition solutions). We obtained an increase of approximately 7-fold in dissolved Ge comparing the deposition solution with blank solution processes for each water concentration (Figure 2d).

Subsequently, the Au-NF morphology and dissolved Ge levels were studied for various SiGe NW alloy compositions (TEM, Figure 3, and ICP-MS, Figure S10 in the Supporting information). The TEM data showed that the Au cap deposition at the NW tip (d$_H$) was constant for the different SiGe NW compositions (Figure 3b). In contrast, the Au deposition length sharply increased for the SiGe composition above approximately 80% Ge (Figure 3c). Notably, the deposition of the gold shell at the tip region was not complete, showing limited surface coverage for NW compositions below approximately 90% Ge, which further support the role of aurophilic interactions, as further discussed below. The CVD process parameters and the corresponding SiGe NW compositions measured for the various NW synthesis processes are provided in the SI (Table S1 and Figure S11 in the Supporting information). The ICP-MS results showed similar trends with an abrupt increase in the dissolved Ge concentration for Ge contents of 70% or more for the deposition and blank solution processes (Figure S10 in the Supporting information). Combining the ICP-MS results for the various NW compositions and water concentrations showed that the Ge dissolution strongly depends on both the SiGe composition and the water concentration. Furthermore, the evo-

lution of the Au cap deposition obtained from TEM imaging and quantification of the dissolved Ge in solution by ICP-MS followed a similar trend with respect to water concentration in the deposition solution. To account for the dissolved Ge levels and the progression of cap deposition, we assumed that an electroless-type metal deposition process occurred in the presence of noble metal cations (Au^{+3}) because of galvanic displacement and metal assisted chemical etching (MACE) mechanisms.[26–31] While SiO$_2$ is a stable oxide that requires relatively harsh etch conditions, such as HF for dissolution, pure GeO$_2$ is prone to dissolution in mild conditions and even in moist environments due to assistance by the MACE mechanism.[32] Therefore, water can be used as a mild etchant for removing the native oxide of Si-Ge alloys. Adjusting the SiGe NW composition tuned the overall stability of the SiGe alloy native oxide towards dissolution in the presence of water to a level where the native oxide is stable towards water dissolution as long as it is decoupled from the metal assisted etch. The removal of the native oxide from the SiGe nanowire surface results in an exposed surface that is prone to undergo a galvanic displacement reaction with Au^{+3} metal ions, generating oxidized SC and resulting in additional Ge dissolution. Generally, MACE promotes SC oxidation near the SC-noble metal junction, where holes accumulate and the gold NP used during the CVD synthesis of the NW function as an electron acceptor, further catalyzing metal deposition at the Au NP surface at the tip of the NW.[30] Namely, the metal-assisted catalytic deposition occurring at the Au catalyst surface is coupled with the MACE process that occurs at the SC portion.[33,34] In addition, the EtOH serves not only as a solvent but also as a reducing agent during the neck deposition step. This was studied by mixtures of tert-butanol-EtOH for the deposition process (Figure S12, Supporting information). Tert-butanol was used as the solvent for these studies because a tertiary alcohol does not take part in the surface redox reactions therefore it acts as a redox-inert solvent system. NF synthesis in neat tert-butanol resulted in Au deposition at the np surface and only sparse metal deposition at the neck up to a well-defined distance from the SC-Au interface at the NW tip (Figure S12a). Addition of EtOH to the tert-butanol solution led to deposited metal tip which evolved gradually with the EtOH fraction showing increase in the Au clusters density and size. These results suggest that Au clusters nucleate at the exposed Ge surface following the MACE removing the native oxide layer at the neck region by galvanic displacement. The nuclei growth is then catalyzed by the oxidation of the EtOH over the Au nuclei surface, where the EtOH function as a reducing agent towards the metal salt. We further demonstrated the role of EtOH not only as solvent but also for promoting the redox reactions by employing several other reducing agents including glucose, phenol, and ascorbic acid, all resulted in NF structures with different morphologies while keeping similar overall dH and L dimensions (Figure S13, Supporting information). The coinage metals and Au in particular are well-known for their catalytic role in promoting the oxidation and dehydrogenation of alcohols.[35,36] Therefore we further studied

the NF synthesis for other metals, including Ag and Cu, which together with Au constitute the coinage metal elements, all showing NF structures with different morphologies as detailed in the sections below (see Figure 7). In contrast, Pd and even Pt salts did not yield such structures, although Pt provides a high driving force for the process, further supporting the role of the coinage metals in surface-catalyzed redox reactions that drive the NF synthesis process. We suggest that the process which is carried out under anaerobic conditions is terminated by the formation of surface-bound species such as Au-H which prevent further metal deposition.[37–39]

Furthermore, we identified a constant ratio of approximately 7 for dissolved Ge for all studied SiGe alloy compositions when analyzing the resulting solutions for deposition and blank (without gold) processes (Figure S10, Supporting information, $R^2 \approx 0.97$). The fixed ratio obtained of 7/1 obtained for the corresponding deposition/blank processes for the various SiGe ratios suggests that a fixed number of redox events with a well-defined stoichiometry take place upon dissolution of the oxide layer and exposure of the pristine SC surface. The surface redox reactions resulted in the deposition of reduced Au^0 clusters at the exposed NW tip region and the oxidation of the SiGe alloy, which was further dissolved into the deposition solution and resulted in the increased Ge levels with fixed proportion. To confirm that the native oxide etch is localized to the NW tip area, dissolved Ge levels were quantified as a function of NW length. The ICP-MS analysis gave constant dissolved Ge levels for all NW growth times, namely, all of the studied NW lengths (SiGe 1:18, Figure S14, Supporting information). This result indicated that dissolved Ge was independent of the NW length and the total NW surface area, which increase linearly with the NW length. This finding agrees with the MACE mechanism, in which the oxide etch is restricted to the metal-SC junction near the NW tip irrespective of the total native oxide layer surface (see Figure S1, Supporting information for the calculated Au-SiGe junction band diagram).[30] Controlling the SiGe alloy composition extends beyond tuning the SiGe alloy native oxide stability towards MACE. To form a metal cap with structural robustness at the exposed NW tip, suitable Au-Au and Au-SC surface interactions are required. Pure Si surfaces exhibit poor adhesion of the reduced metal clusters relative to Ge.[28] Furthermore, it was previously reported for Ge surfaces that Au-Ge covalently binds with a well-defined stoichiometry.[15] Thus, tuning the SiGe alloy composition also plays a role in the formation of aurophilic interactions, subsequent formation of Au-Ge and Au-Au and stabilization of the reduced metal at the tip region.[40]
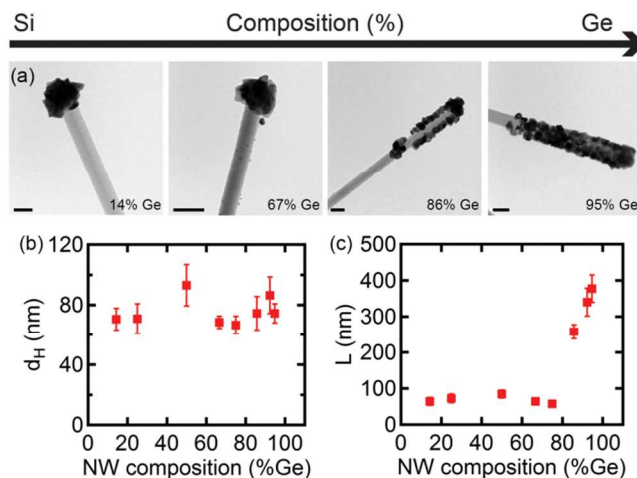

Figure 3. Au-NF structures obtained for various SiGe NW compositions. (a) Left to right: TEM images of the Au-NF obtained using 14%, 67%, 86% and 95% Ge/Si NWs (scale bars represent 50 nm). (b) Au cap diameter and (c) Au cap length as a function of the NW composition.
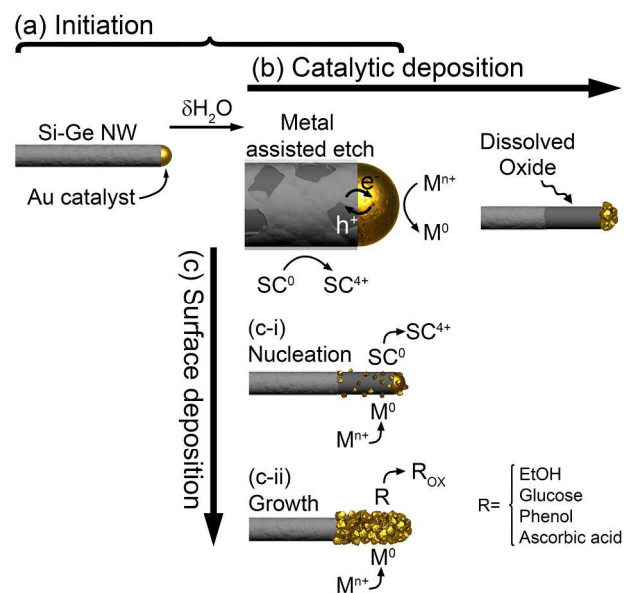

Figure 4. Summary of Au-NF hybrid nanostructure synthesis and the mechanism for SiGe alloy nanowires (SiGe NWs). (a) Process initiation by mild etching using water that removes the SiGe alloy oxide layer at the SC-metal (Au) tip region. (b) Catalytic metal deposition at the Au catalyst edge. (c) Metal deposition at the exposed SiGe NW surface tip region. The SiGe alloy native oxide layer is locally removed in the presence of water by metal-assisted chemical etching due to the SC-Au junction that is inherently present at the CVD synthesized NW edge. Galvanic redox reactions at the exposed SC tip region result in metal cation reduction and nucleation. Metal clusters grow at the nuclei assisted by the catalytic redox reactions driven by the reducing agent (R). This process stops when the exposed SC at the tip region is completely covered with a metal layer, probably involving surface poisoning with Au-H species at the anaerobic conditions of the synthesis which results in a self-limiting process.

Overall, the Au-NF synthesis involves a sequence of localized etching of the SC oxide layer and self-limiting metal deposition to yield Au° cap deposition with well-defined dimensions at the NW tip. The cap deposition process involves two metal deposition mechanisms, direct galvanic displacement at the exposed SC surface and catalytic metal deposition, metal-assisted catalytic deposition, at the nanowire tip, resulting in dissolved Ge in the solution, and self termination of the process upon full coverage of the exposed SC region. A summary of the NF synthesis mechanisms and various processes is presented in Figure 4.

Additional fine-tuning of the Au-NF structures morphology was demonstrated for controlling the size of deposited Au clusters by adding alkylthiols to the Au-NF process solution. Au-NF prepared using the same procedure while adding 5 mM hexanethiol in the deposition solution result in a significantly smaller average Au cluster size (3 ± 0.3 nm) compared with Au-NFs prepared in the absence of hexanethiol (17 ± 3 nm) (Figure 5). The smaller cluster size with hexanethiol molecules resulted because thiols were bound with the freshly formed Au clusters and formed a self-assembled monolayer that function as a passivation layer on the pristine Au clusters.
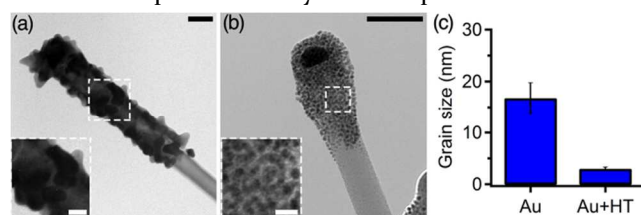

Figure 5. Au-NF cluster size and morphology tuning. (a) TEM images of Au-NF structures obtained without thiol, and (b) with 5 mM hexanethiol. Both preparations were with 1 mM $AuCl_3$ and 1.62 M H_2O in EtOH. Scale bars 50 nm and 20 nm (insets). (c) grain size analysis obtained for Au-NF deposition with and without hexanethiol.

The thiol self-assembled monolayer formed *in situ* during Au-NF synthesis, blocking electron transfer and halting cluster growth.[41] Furthermore, binding of the hexanethiol molecules at the freshly formed Au cluster surface diminished the aurophilic interactions and subsequent Au-Au bond formation.[40]

The synthesis of Au/SiGe HNS progression was directly followed by *in situ* scanning transmission electron microscopy (STEM) using a novel fluid cell TEM holder. This technique uses a high angular annular dark field (HAADF) detector to provide the atomic mass or Z-contrast. Cap formation was initiated by introducing water to the Au salt solution that was dissolved in EtOH prior to the injection into the liquid cell holder (Figure S15 in the Supporting information) A continuous increase of intensity could be observed once the reaction commenced and after 300 s the intensity increased by a factor of two with an increase of the tip diameter from 30 nm to 45 nm as measures by line profiles across the wire tip (Figure S15c). Imaging was performed using a low dose of 5 e⁻/nm² allowing for a direct observation of the synthesis

in solution without triggering secondary Au formation due to the electron beam interaction with the solution as observed e.g. for plane wave TEM imaging where electron doses are several orders of magnitude higher.[42] The image intensity reflects the growing tip thickness since it is related to Rutherford scattering which scales with the sample thickness. Metal cap deposition was found to be confined to a length of approx. 350 nm in line with the post mortem TEM images shown in Figure 2c for this system.

Overall, our results revealed that distinct processing steps can be identified that are analogous to those of conventional top-down processing, as depicted in Figure 6. The structures are formed using a self-propagating sequence that includes etching, deposition, modification and self-termination of the transformations.
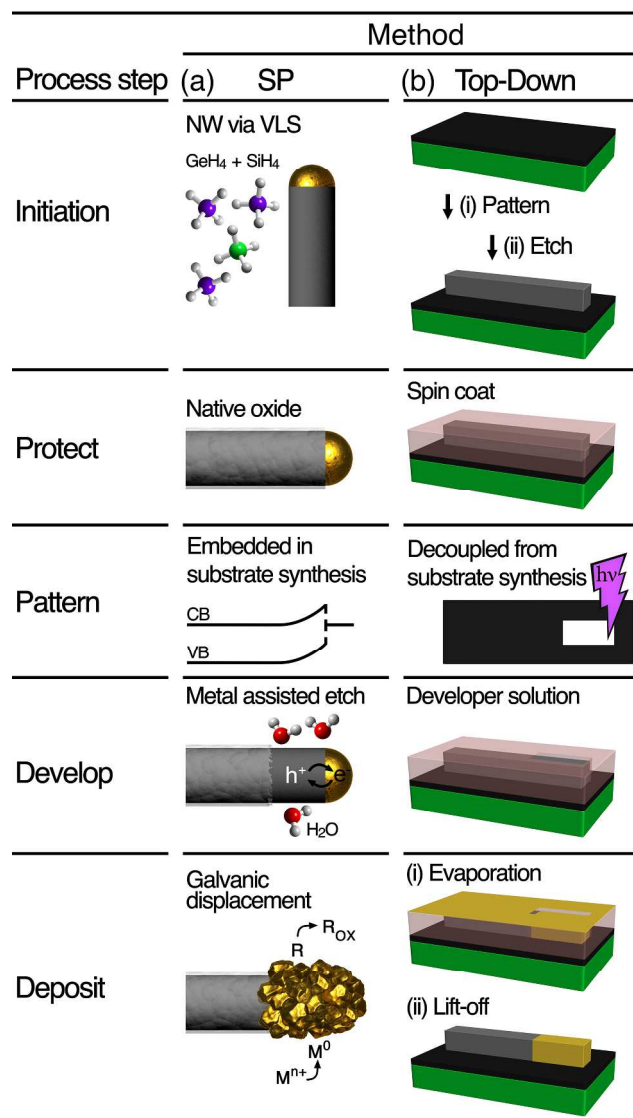

Figure 6. Fabrication of SC-metal hybrid nanostructures. Using (a) self-processing synthesis and (b) conventional top-down processing sequence.

The scope of NF synthesis was further generalized to depositing Ag and Cu. Together with Au, these metals constitute the coinage metal group (row 11 of the periodic

table). The silver deposited NF, Ag-NF, had a similar morphology to that of the Au-NF with a metal cap deposited at the NW tip near the SC-Au NP junction region (Figure 7a). The diameter of the deposited Ag head (d_H) was ~130 nm for all of the studied water concentrations, except for the anhydrous solution, in which nearly no such deposition was observed (Figure 7a-iii). An Ag cap deposition length (L) of ~300 nm was obtained for all of the water concentrations, except for the anhydrous solution, in which no significant deposition was observed (Figure 7a-iv). For copper deposited NF, Cu-NF resulted in a distinct morphology compared with Au- and Ag-NF. In addition, Cu-NF displayed a spherical structure and its d_H and L increased as water concentration increased and became saturated at ~110 nm (Figure 7b). This result could be attributed to the lower standard redox potentials of Cu^{+2} compared with the other metals studied here ($E°(Cu^{2+}/Cu)$= +0.340 V, $E°(Ag^+/Ag)$=+0.799 V, and $E°(Au^{3+}/Au)$=+1.498 V).[43] We suggest that the reduction of Cu^{2+} to Cu^o is restricted to the SC-Au NP surface by metal-assisted catalytic deposition and occurs at the Au tip of the SiGe NW. Namely, the SiGe-Au junction catalyzes Cu^{2+} reduction and deposition by promoting the accumulation of holes at the SC-noble metal interface and injection of electrons to the Au catalyst surface. The lower standard redox potential for Cu only results in deposition *via* metal-assisted catalytic deposition because the driving force for the direct galvanic displacement process is not sufficient. In contrast, for Au- and Ag-NF, the standard redox potential is sufficiently positive for activating the direct galvanic displacement at the exposed SC interface (where the native oxide is removed by MACE) and the metal-assisted catalytic deposition mechanism at the NW-tip. Finally, the formation of bi-metallic NF structures was achieved by step-wise deposition of (Au, Ag)-NF and (Au, Cu)-NF, as shown in Figures. 7c and 7d, respectively. Notably, Ag and Cu-NF exhibit properties that could be further exploited in the future.[44-48]
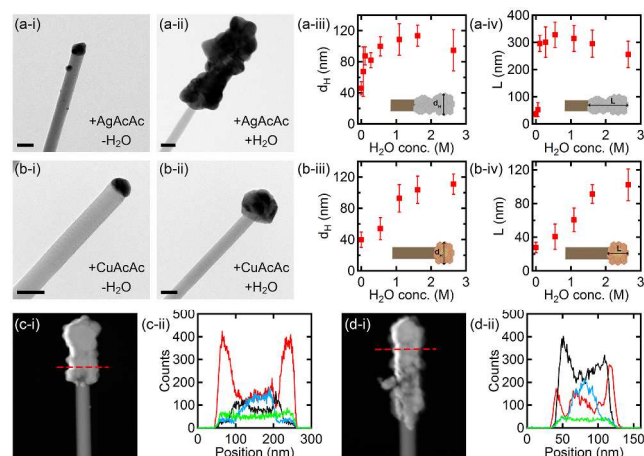

Figure 7. Synthesis of coinage metal (Cu, Ag, and Au)-NF structures. (a) TEM images obtained for Ag-NF prepared in anhydrous EtOH/acetonitrile solution (a-i) and in 1 M of H_2O in EtOH/acetonitrile solution (a-ii). Evolution of the Ag tip as a function of the H_2O concentration, tip diameter (a-iii) and tip length (a-iv). (b) TEM images obtained for Cu-NF prepared in an anhydrous EtOH/DCM solution (b-i) and in EtOH/DCM with 2.64 M of H_2O (b-ii). The Cu tip evolved as a function of the H_2O concentration, tip diameter (b-iii) and tip length (b-iv). The scale bar is 50 nm for all of the TEM images. (c) The step by step deposition of bimetallic (Au, Ag)-NF prepared with 1.62 M of H_2O, (c-i) The STEM image and (c-ii) the corresponding EDS profile measured along the broken line (Ag-red, Au-black, Ge-blue and Si-green). (d) Step by step deposition of bimetallic (Au, Cu)-NF prepared with 1.62 M of H_2O, (d-i) the STEM image, and (d-ii) the corresponding EDS profile measured along the broken line (Cu-red, Au-black, Ge-blue and Si-green).

The optical absorbency of the NF films was measured on quartz slides using an integrating sphere showing a broad plasmonic band (Figure S16). The plasmon resonance of the metallic NF nanostructures exhibit significant local electromagnetic field enhancement which is the origin of the enhancement in SERS.[49] Metallic nano structures are well known for their utility in probing adsorbed probe molecules with high amplification of the Raman signal commonly termed SERS.[50] We utilize the plasmonic absorption to demonstrate the application of NF films as SERS substrates using thiophenol monolayer. Raman spectra measured for thiophenol-functionalized Au-NF, Ag-NF, and (Au,Ag)-NF are presented in Figure 8. The SERS signals obtained for monolayer of thiophenol were detected for Au-, Ag-, and (Au,Ag)-NF with the highest SERS signal obtained for the bi-metallic (Au,Ag)-NF. In contrast, for NW films treated with the thiophenol molecules no Raman signals could be detected (Figure S16d). Furthermore, the SERS intensity obtained for Au-NF was studied for three excitation wavelengths, 355, 514, and 785 nm. The SERS signal enhancement was obtained for 785nm in close relation to the plasmonic absorption onset at 701nm shown in Figure S16b. Excitation at shorter wavelengths, 355 and 514nm which do not overlap with the plasmonic band did not result in SERS signals (Figure S16c). Additional optical absorbency and Raman measurements of control samples can be found in the supporting information, Figure S16.
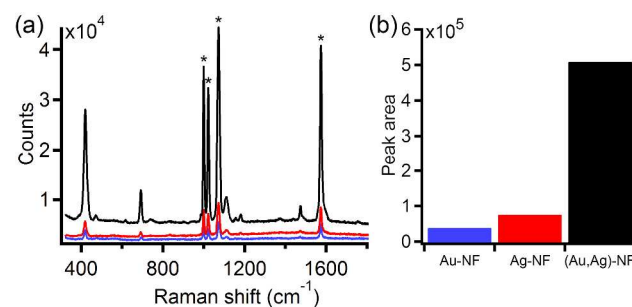

Figure 8 SERS enhancement of thiophenol over NF films. (a) Raman spectra measured for Au-NF (blue), Ag-NF (red), and (Au,Ag)-NF (black). The four main peaks of thiophenol are designated by '*' at 1000, 1024, 1072, and 1574 cm^{-1}. (b) Corresponding integrated peak area of the 1072 cm^{-1} peak shown in (a).

CONCLUSIONS

1
2
3
4
5
6
7
8
9
10
11
12
13
14
15
16
17
18
19
20
21
22
23
24
25
26
27
28
29
30
31
32
33
34
35
36
37
38
39
40
41
42
43
44
45
46
47
48
49
50
51
52
53
54
55
56
57
58
59
60

In summary, we present a synthetic strategy that takes advantage of the inherent asymmetry of the NW structure with the SiGe-Au NP seed left from the CVD process and the vapor-liquid-solid (VLS) synthesis mechanism.[51–53] The SiGe-Au junction is used for activating etching, deposition, and modification steps. Control over the deposition and etching processes has been demonstrated by several parameters: (i) etchant concentration (water), (ii) SiGe alloy composition, (iii) reducing agents, (iv) metal redox potential, and (v) addition of surfactants for controlling grain size. Both the etching and deposition processes were confined to a well-defined region of the structure with self-limiting reactions. These traits allowed for structural control that is typically associated with top-down fabrication capabilities. We demonstrated that the bottom-up synthesis involves a sequence of multiple steps cued by the local etching (MACE) of the SiGe alloy oxide layer, catalytic deposition of metal cations at the NW tip by metal-assisted catalytic deposition, and deposition at the exposed NW tip by galvanic displacement. The method was demonstrated here to the coinage metals, Cu, Ag, and Au, while the synthesis with other metals such as Pd and Pt did not result in NF structures. Introducing surfactants (hexanethiol) allowed further control over the deposited cluster size and morphology. Finally, we demonstrated the syntheses of bimetallic NFs when employing the coinage metals Au, Ag, and Cu. These bimetallic building blocks are highly attractive for catalysis, optical applications, SERS, and more. The overall synthesis is termed self-processing due to the controllable, localized, and self-limiting sequence of events executed autonomously resulting in the transformation of the SiGe NW structure into nano-flora-like hybrid nanostructures. In addition, the self-processing strategy demonstrated here for NF-HNS architectures enables interesting possibilities regarding controlled symmetry breaking at the nanoscale, which is an important feature for attaining complex nanosystems with intriguing functionalities. Such HNSs consist of metal and SC with distinct dimensionalities that encompass significant effects in a wide range of applications, such as photocatalysis, photovoltaics, sensing, energy harvesting and storage, and electronic devices.[44–46,54–57]

METHODS

Synthesis of Silicon-Germanium (Si–Ge) alloy nanowire (NW): Glass slides were cleaned using O_2 plasma (Pico plasma cleaner, Diener electronic GmbH) at 60 W for 2 min. Next, the slides were immediately incubated for 5 min in a poly-L lysine solution (0.1% in H_2O, Sigma-Aldrich) before being washed with ultra pure DI water (>18 MΩ, ELGA purification system). Then, Au NPs were deposited from a citrate-stabilized water suspension (Ted Pella Inc.) and washed with DI water. The slides were then cleaned using O_2 plasma to remove any organic residues and contaminants. The NW synthesis was conducted using a custom-built CVD system. In addition, SiGe NWs with various alloy compositions were obtained by varying the appropriate process flow parameters for GeH_4 (10% in H_2) and pure SiH_4 for specified time durations. The spe-

cific process parameters for the various SiGe alloys are provided in Table S1.

SiGe nano-floret (NF) synthesis: First, SiGe alloy NWs were prepared on substrates and stored in an ambient atmosphere for 24 hr to form a native oxide layer. Then, Au-NFs were prepared by reacting the substrates with NWs in an EtOH solution (99%, ACROS Organics) containing 1 mM $AuCl_3$ (99%, ACROS Organics) and a specified water content for 3 min at room temperature. The treated substrates were carefully washed with EtOH and TDW to remove excess salts. Next, Ag-NFs were prepared using the same procedure with 5 mM silver acetylacetonate (98%, Aldrich) in EtOH/acetonitrile 1/1 (v/v) (≥99.9% Merck). Then, Cu-NFs were prepared using a 10 mM copper acetylacetonate (98%, ACROS Organics) solution with EtOH/DCM 1/1 (v/v) (≥99.8%, Sigma-Aldrich) and at the specified water content. Deposition with different reducing agents was conducted by using anhydrous tert-butnaol (Aldrich) as solvent for the above deposition solution with the addition of the specified amount of anhydrous MeOH, anhydrous EtOH, glucose, phenol, or ascorbic acid to the deposition solution.

Transmission electron microscopy (TEM): First, NW and NF were synthesized directly on TEM grids with 50 nm silicon nitride support films (Ted Pella Inc.) following the NF synthesis procedure described above. Then, TEM and STEM imaging were performed using an FEI Tecnai F20 G^2 microscope with EDAX EDS detector.

Fluid cell scanning transmission electron microscopy (STEM): In situ observations of the Au growth on SiGe nanowires were performed using a Poseidon 200 fluid cell transmission electron microscopy holder (Protochips Inc.) in a double Cs-corrected JEOL 2200 FS microscope operated at 200 kV acceleration voltage in scanning mode using a high-annular angular X-ray detector. The 3C probe setting and the smallest condenser aperture were used to optimize the contrast and resolution.

For these studies, two Si chips with a 50 nm thick silicon nitride membrane each were employed using a spacer thickness of 500 nm (minimum fluid layer thickness in the beam direction) to separate the two chips. Before the observations, the SiGe nanowires were deposited on the lower chip. The experiment was performed using first an anhydrous EtOH solution, pumped at a rate of 300 μl/hr, before the 1 mM Au/EtOH solution was introduced after approximately 30 minutes using the same pump rate. Suitable nanowires were selected prior to the addition of the Au containing solution. After adding the Au/EtOH solution, the sample was imaged at low magnification (20 k) to minimize beam-induced reactions. The Au growth related increase of intensity at the NW tips occurred approx. 15 min after injection of the Au containing solution corresponding.

Optical absorbency measurements were performed using a PerkinElmer Lambda 1050 spectrometer with an integrating sphere.

Raman spectroscopy was measured using Renishaw in-Via Reflex Spectrometer using 785 nm diode laser for ex-

citation unless otherwise specified. Excitation power used was 0.3 µW and spot size of 1.2 µm. Measurements were performed on NF films prepared on thin microscope glass slides. Excitation of approximately 10 NF structures is estimated for this beam spot size based on average film density evaluated by SEM imaging.

ASSOCIATED CONTENT

Supporting Information. Figures S1-S16, Table S1. This material is available free of charge via the Internet at http://pubs.acs.org

AUTHOR INFORMATION

Corresponding Author

* roie.yerushalmi@mail.huji.ac.il

Present Addresses

† Department of Chemistry, Chikkaiah Naicker College, Erode-638004, Tamilnadu, India.

Author Contributions

‡These authors contributed equally.

ACKNOWLEDGMENT

REFERENCES

(1)   McGuire, G. E. *Semiconductor Materials and Process Technology Handbook: For Very Large Scale Integration (VLSI) and Ultra Large Scale Integration (ULSI);* Noyes Publications: Park Ridge, N.J., U.S.A., 1988.

(2)   Koch, C. C. *Nanostructured Materials Processing, Properties, and Applications;* Second.; William Andrew Pub.: Norwich, N.Y., U.S.A., 2007.

(3)   Cölfen, H.; Mann, S. *Angew. Chem. Int. Ed. Engl.* **2003**, 42, 2350.

(4)   Costi, R.; Saunders, A. E.; Banin, U. *Angew. Chem. Int. Ed. Engl.* **2010**, 49, 4878.

(5)   Reddy, A. L. M.; Gowda, S. R.; Shaijumon, M. M.; Ajayan, P. M. *Adv. Mater.* **2012**, 24, 5045.

(6)   Walther, A.; Müller, A. H. E. *Chem. Rev.* **2013**, 113, 5194.

(7)   Loget, G.; Kuhn, A. *J. Mater. Chem.* **2012**, 22, 15457.

(8)   Zeeshan, M. A.; Shou, K.; Pané, S.; Pellicer, E.; Sort, J.; Sivaraman, K. M.; Baró, M. D.; Nelson, B. J. *Nanotechnology* **2011**, 22, 275713.

(9)   Jia, G.; Sitt, A.; Hitin, G. B.; Hadar, I.; Bekenstein, Y.; Amit, Y.; Popov, I.; Banin, U. *Nat. Mater.* **2014**, 13, 301.

(10)   Kurppa, K.; Jiang, H.; Szilvay, G. R.; Nasibulin, A. G.; Kauppinen, E. I.; Linder, M. B. *Angew. Chemie* **2007**, 119, 6566.

(11)   Fischer, V.; Lieberwirth, I.; Jakob, G.; Landfester, K.; Muñoz-Espí, R. *Adv. Funct. Mater.* **2013**, 23, 451.

(12)   Xu, C.; Zeng, Y.; Rui, X.; Xiao, N.; Zhu, J.; Zhang, W.; Chen, J.; Liu, W.; Tan, H.; Hng, H. H.; Yan, Q. *ACS Nano* **2012**, 6, 4713.

(13)   Touahir, L.; Galopin, E.; Boukherroub, R.; Gouget-Laemmel, A. C.; Chazalviel, J.-N.; Ozanam, F.; Saison, O.; Akjouj, A.; Pennec, Y.; Djafari-Rouhani, B.; Szunerits, S. *Analyst* **2011**, 136, 1859.

(14)   Halouzka, V.; Jakubec, P.; Kvitek, L.; Likodimos, V.; Kontos, A. G.; Papadopoulos, K.; Falaras, P.; Hrbac, J. *J. Electrochem. Soc.* **2013**, 160, B54.

(15)   Wipf, M.; Stoop, R. L.; Tarasov, A.; Bedner, K.; Fu, W.; Wright, I. A.; Martin, C. J.; Constable, E. C.; Calame, M.; Schönenberger, C. *ACS Nano* **2013**, 7, 5978.

(16)   Zhang, B.; Wang, H.; Lu, L.; Ai, K.; Zhang, G.; Cheng, X. *Adv. Funct. Mater.* **2008**, 18, 2348.

(17)   Yilmaz, M.; Senlik, E.; Biskin, E.; Yavuz, M. S.; Tamer, U.; Demirel, G. *Phys. Chem. Chem. Phys.* **2014**, 16, 5563.

(18)   Banan Sadeghian, R.; Islam, M. S.; Saif Islam, M. *Nat. Mater.* **2011**, 10, 135.

(19)   Qu, Y.; Xue, T.; Zhong, X.; Lin, Y.-C.; Liao, L.; Choi, J.; Duan, X. *Adv. Funct. Mater.* **2010**, 20, 3005.

(20)   Ouyang, S.; Kikugawa, N.; Zou, Z.; Ye, *J. Appl. Catal. A Gen.* **2009**, 366, 309.

(21)   Talafi Noghani, M.; Vadjed Samiei, M. H. *Plasmonics* **2013**, 8, 1155.

(22)   Paniagua-Domínguez, R.; Abujetas, D. R.; Sánchez-Gil, J. A. *Sci. Rep.* **2013**, 3, 1507.

(23)   Ghosh, H.; Bouhekka, A.; Bürgi, T. *Phys. Chem. Chem. Phys.* **2014**, 16, 19402.

(24)   Recio-Sánchez, G.; Namura, K.; Suzuki, M.; Martín-Palma, R. J. *Nanoscale Res. Lett.* **2014**, 9, 487.

(25)   Gaiduk, P. I.; Larsen, A. N. *Phys. status solidi* **2014**, 211, 2455.

(26)   Porter, L. A.; Choi, H. C.; Ribbe, A. E.; Buriak, J. M. *Nano Lett.* **2002**, 2, 1067.

(27)   Sayed, S. Y.; Wang, F.; Malac, M.; Meldrum, A.; Egerton, R. F.; Buriak, J. M. *ACS Nano* **2009**, 3, 2809.

(28)   Magagnin, L.; Maboudian, R.; Carraro, C. *J. Phys. Chem. B* **2002**, 106, 401.

(29)   Fabre, B.; Hennous, L.; Ababou-Girard, S.; Meriadec, C. *ACS Appl. Mater. Interfaces* **2013**, 5, 338.

(30)   Huang, Z.; Geyer, N.; Werner, P.; de Boor, J.; Gösele, U. *Adv. Mater.* **2011**, 23, 285.

(31)   Zuo, Z.; Cui, G.; Shi, Y.; Liu, Y.; Ji, G. *Nanoscale Res. Lett.* **2013**, 8, 193.

(32)   Murthy, M. K.; Hill, H. *J. Am. Ceram. Soc.* **1965**, 48, 109.

(33)   Nassiopoulou, A. G.; Gianneta, V.; Katsogridakis, C. *Nanoscale Res. Lett.* **2011**, 6, 597.

(34)   Bang, B. M.; Kim, H. J.; Park, S. J. *Electrochem. Sci. Technol.* **2011**, 2, 157.

(35)   Syu, C.-Y.; Yang, H.-W.; Hsu, F.-H.; Wang, J.-H. *Phys. Chem. Chem. Phys.* **2014**, 16, 7481.

(36)   Liu, X.; Madix, R. J.; Friend, C. M. *Chem. Soc. Rev.* **2008**, 37, 2243.

(37)   Manzoli, M.; Chiorino, A.; Vindigni, F.; Boccuzzi, F. *Catal. Today* **2012**, 181, 62.

(38)   Maldotti, A.; Molinari, A.; Juárez, R.; Garcia, H. *Chem. Sci.* **2011**, 2, 1831.

(39)   Zaccheria, F.; Ravasio, N.; Psaro, R.; Fusi, A. *Chem. Commun.* **2005**, 253.

(40)   Schmidbaur, H. *Chem. Soc. Rev.* **1995**, 24, 391.

(41)   Pensa, E.; Cortés, E.; Corthey, G.; Carro, P.; Vericat, C.; Fonticelli, M. H.; Benítez, G.; Rubert, A. A.; Salvarezza, R. C. *Acc. Chem. Res.* **2012**, 45, 1183.

(42)   Abellan, P.; Woehl, T. J.; Parent, L. R.; Browning, N. D.; Evans, J. E.; Arslan, I. *Chem. Commun.* **2014**, 50, 4873.

(43)   Bard, A. J.; Parsons, R.; Jordan, J. *Standard Potentials in Aqueous Solution;* M. Dekker: New York, 1985.

(44)   Lu, Q.; Lu, Z.; Lu, Y.; Lv, L.; Ning, Y.; Yu, H.; Hou, Y.; Yin, Y. *Nano Lett.* **2013**, 13, 5698.

(45)   Carotenuto, G.; Pepe, G. P.; Nicolais, L. *Eur. Phys. J. B* **2000**, 16, 11.

(46)   Wu, Y.; Wadia, C.; Ma, W.; Sadtler, B.; Alivisatos, A. P. *Nano Lett.* **2008**, 8, 2551.

(47)   Kim, J. S.; Kuk, E.; Yu, K. N.; Kim, J.-H.; Park, S. J.; Lee, H. J.; Kim, S. H.; Park, Y. K.; Park, Y. H.; Hwang, C.-Y.; Kim, Y.-K.; Lee, Y.-S.; Jeong, D. H.; Cho, M.-H. *Nanomedicine* **2007**, 3, 95.

(48)   Lim, S.; Joyce, M.; Fleming, P. D.; Aijazi, A. T.; Atashbar, M. *J. Imaging Sci. Technol.* **2013**, 57, 50506.

(49)   Tao, A.; Kim, F.; Hess, C.; Goldberger, J.; He, R.; Sun, Y.; Xia, Y.; Yang, P. *Nano Lett.* **2003**, 3, 1229.

(50)   Ru, E. Le; Etchegoin, P. *Principles of Surface-Enhanced Raman Spectroscopy: and related plasmonic effects;* Elsevier, 2008.

(51)   Wagner, R. S.; Ellis, W. C. *Trans. Metall. Soc. AIME* **1965**, 233, 1053.

(52)   Cui, Y.; Lauhon, L. J.; Gudiksen, M. S.; Wang, J.; Lieber, C. M. *Appl. Phys. Lett.* **2001**, 78, 2214.

(53)   Schwalbach, E. J.; Voorhees, P. W. *Nano Lett.* **2008**, 8, 3739.

(54)   Jia, X.; Hu, G.; Nitze, F.; Barzegar, H. R.; Sharifi, T.; Tai, C.-W.; Wågberg, T. *ACS Appl. Mater. Interfaces* **2013**, 5, 12017.

(55)   Zhang, Q.; Uchaker, E.; Candelaria, S. L.; Cao, G. *Chem. Soc. Rev.* **2013**, 42, 3127.

(56)   Zhu, C.; Dong, S. *Nanoscale* **2013**, 5, 10765.

(57)   Kumar, B.; Lee, K. Y.; Park, H.-K.; Chae, S. J.; Lee, Y. H.; Kim, S.-W. *ACS Nano* **2011**, 5, 4197.

SYNOPSIS TOC.